43. Baker, V. C. The Channels on Mars (Univ. Texas Press, Austin, 1982).
44. Moore, J. M., Howard, A. D., Dietrich, W. E. & Schenk, P. M. Martian layered fluvial deposits: implications for Noachian climate scenarios. Geophys. Res. Lett. 30, doi:10.1029/2003GL019002 (2003).
45. Malin, M. C. & Edgett, K. S. Evidence for persistent flow and aqueous sedimentation on early Mars. Science 302, 1931–1934 (2003).
46. Bhattacharya, J. P., Payenberg, T. H. D., Lang, S. C. & Bourke, M. Dynamic river channels suggest a long-lived Noachian crater lake on Mars. Geophys. Res. Lett. 32, doi:10.1029/2005GL022747 (2005).
47. Kleidon, A., Fraedrich, K. & Heimann, M. A green planet versus a desert world: Estimating the maximum effect of vegetation on the land surface climate. Clim. Change 44, 471–493 (2000).
48. Hilley, G. E. & Strecker, M. R. Steady-state erosion of critical Coulomb wedges with applications to Taiwan and the Himalaya. J. Geophys. Res. 109, B01411, doi:10.1029/2002JB002284 (2004).
49. Whipple, K. X. & Meade, B. J. Controls on the strength of coupling among climate, erosion, and deformation in two-sided, frictional orogenic wedges at steady state. J. Geophys. Res. 109, F01011, doi:10.1029/2003JF000019 (2004).
50. Richards, M. A., Yang, W. S., Baumgardner, J. R. & Bunge, H. P. Role of a low-viscosity zone in stabilizing plate tectonics: Implications for comparative terrestrial planetology. Geochem. Geophys. Geosyst. 2, doi:10.1029/2000GC000115 (2001).
51. Nimmo, F. & McKenzie, D. Volcanism and tectonics on Venus. Annu. Rev. Earth Planet. Sci. 26, 23–51 (1998).
52. Chyba, C. F. Rethinking Earth's early atmosphere. Science 308, 962–963 (2005).
53. Baker, V. R. Water and the martian landscape. Nature 412, 228–236 (2001).
54. Craddock, R. A. & Howard, A. D. The case for rainfall on a warm, wet early Mars. J. Geophys. Res. 107, doi:10.1029/2001JE001505 (2002).
55. Irwin, R. P., Craddock, R. A. & Howard, A. D. Interior channels in Martian valley networks: Discharge and runoff production. Geology 33, 489–492 (2005).
56. Howard, A. D., Moore, J. M. & Irwin, R. P. III An intense terminal epoch of widespread fluvial activity on early Mars: 1. Valley network incision and associated deposits. J. Geophys. Res. 110, doi:10.1029/2005JE002459 (2005).
57. Head, J. W. et al. Tropical to mid-latitude snow and ice accumulation, flow and glaciation on Mars. Nature 434, 346–351 (2005).
58. Piqueux, S., Byrne, S. & Richardson, M. I. Sublimation of Mars's southern seasonal CO₂ ice cap and the formation of spiders. J. Geophys. Res. 108, doi:10.1029/2002JE002007 (2003).
59. Byrne, S. & Ingersoll, A. P. A sublimation model for Martian South Polar ice features. Science 299, 1051–1053 (2003).
60. Tomasko, M. G. et al. Rain, winds and haze during the Huygens probe's descent to Titan's surface. Nature 438, 765–778 (2005).
61. Willgoose, G. A statistic for testing the elevation characteristics of landscape simulation models. J. Geophys. Res. 99, 13987–13996 (1994).
62. Stock, J. D. & Dietrich, W. E. Valley incision by debris flows: evidence of a topographic signature. Wat. Resour. Res. 39, 1089, doi:10.1029/2001WR001057 (2003).
63. McEwen, A. et al. MRO's High Resolution Imaging Science Experiment (HIRISE): Science expectations. Sixth Int. Conf. on Mars 3217 (2003); (http://www.lpi.usra.edu/meetings/sixthmars2003/) (2003).
64. Yoo, K., Amundson, R., Heimsath, A. M. & Dietrich, W. E. Process-based model linking pocket gopher (Thomomys bottae) activity to sediment transport and soil thickness. Geology 33, 917–920 (2005).
65. Gabet, E. & Dunne, T. A stochastic sediment delivery model for a steep Mediterranean landscape. Wat. Resour. Res. 39, 1237, doi:10.1029/2003WR002341 (2003).
66. Roering, J. J. & Gerber, M. Fire and the evolution of steep, soil-mantled landscapes. Geology 33, 349–352 (2005).
67. Ahnert, F. in L'evolution des Versants (ed. Macar, P.) 23–41 (Univ. Liege, Liege, France, 1967).
68. Cox, N. J. On the relationship between bedrock lowering and regolith thickness. Earth Surf. Process. Landforms 5, 271–274 (1980).
69. Anderson, R. S. Modeling the tor-dotted crests, bedrock edges, and parabolic

profiles of high alpine surfaces of the Wind River Range, Wyoming. Geomorphology 46, 35–58 (2002).
70. Culling, W. E. H. Analytical theory of erosion. J. Geol. 68, 336–344 (1960).
71. Perron, J. T., Dietrich, W. E., Howard, A. D., McKean, J. A. & Pettinga, J. Ice-driven creep on Martian debris slopes. Geophys. Res. Lett. 30, 1747, doi:10.1029/2003GL017603 (2003).
72. Iverson, R. M. Unsteady, nonuniform landslide motion, 2. Linearized theory and the kinematics of transient-response. J. Geol. 94, 349–364 (1986).
73. Densmore, A. L., Ellis, M. A. & Anderson, R. S. Landsliding and the evolution of normal-fault-bounded mountains. J. Geophys. Res. 103, 15203–15219 (1998).
74. Iverson, R. M. Regulation of landslide motion by dilatancy and pore pressure feedback. J. Geophys. Res. 110, doi:10.1029/2004JF000268 (2005).
75. Stock, J. D. Incision of Steepland Valleys by Debris Flows Ph.D. thesis, Univ. California, Berkeley (2003).
76. MacGregor, K. R., Anderson, R. S., Anderson, S. P. & Waddington, E. D. Numerical simulations of glacial-valley longitudinal profile evolution. Geology 28, 1031–1034 (2000).
77. Hildes, D. H. D., Clarke, G. K. C., Flowers, G. E. & Marshall, S. J. Subglacial erosion and englacial sediment transport modelled for North American ice sheets. Quat. Sci. Rev. 23, 409–430 (2004).
78. Bagnold, R. A. The Physics of Blown Sand and Desert Dunes (Methuen, London, 1941).
79. Werner, B. T. A steady state model of wind-blown sand transport. J. Geol. 98, 1–17 (1990).
80. McEwan, I. K. The Physics of Sand Transport by Wind Ph.D. thesis, Univ. Aberdeen (1991).
81. Anderson, R. S. Erosion profiles due to particles entrained by wind: Application of an eolian sediment-transport model. Geol. Soc. Am. Bull. 97, 1270–1278 (1986).
82. Lancaster, N. & Baas, A. Influence of vegetation cover on sand transport by wind: field studies at Owens Lake, California. Earth Surf. Process. Landforms 23, 69–82 (1998).
83. Sleep, N. H. & Zahnle, K. Carbon dioxide cycling and implications for climate on ancient Earth. J. Geophys. Res. 106, 1373–1400 (2001).
84. Kump, L. R., Brantley, S. L. & Arthur, M. A. Chemical weathering, atmospheric CO₂, and climate. Annu. Rev. Earth Planet. Sci. 28, 611–667 (2000).
85. Kasting, J. F. & Catling, D. Evolution of a habitable planet. Annu. Rev. Astron. Astrophys. 41, 429–463 (2003).
86. Brasier, M., Green, O., Lindsay, J. & Steele, A. Earth's oldest (~3.5 Ga) fossils and the 'Early Eden hypothesis': questioning the evidence. Orig. Life Evol. Biosph. 34, 257–269 (2004).
87. Bekker, A. et al. Dating the rise of atmospheric oxygen. Nature 427, 117–120 (2004).
88. Tian, F., Toon, O. B., Pavlov, A. A. & De Sterck, H. A hydrogen-rich early Earth atmosphere. Science 308, 1014–1017 (2005).
89. Schrag, D. P., Berner, R. A., Hoffman, P. F. & Halverson, G. P. On the initiation of snowball Earth. Geochem. Geophys. Geosyst. 3, doi:10.1029/2001GC000219 (2002).
90. Edmond, J. M. & Huh, Y. Non-steady carbonate recycling and implications for the evolution of atmospheric PCO₂. Earth Planet. Sci. Lett. 216, 125–139 (2003).

---

# ARTICLES

# Atomic packing and short-to-medium-range order in metallic glasses

H. W. Sheng[1], W. K. Luo[1], F. M. Alamgir[2], J. M. Bai[3] & E. Ma[1]

Unlike the well-defined long-range order that characterizes crystalline metals, the atomic arrangements in amorphous alloys remain mysterious at present. Despite intense research activity on metallic glasses and relentless pursuit of their structural description, the details of how the atoms are packed in amorphous metals are generally far less understood than for the case of network-forming glasses. Here we use a combination of state-of-the-art experimental and computational techniques to resolve the atomic-level structure of amorphous alloys. By analysing a range of model binary systems that involve different chemistry and atomic size ratios, we elucidate the different types of short-range order as well as the nature of the medium-range order. Our findings provide a reality check for the atomic structural models proposed over the years, and have implications for understanding the nature, forming ability and properties of metallic glasses.

Historically, a widely cited structural model for metallic glasses (MGs) is that of Bernal's dense random packing of hard spheres[1,2]. It is now understood that Bernal's idea can satisfactorily model monatomic systems (or alloys with constituent species having comparable atomic sizes and insignificant chemical short-range order, SRO)[3], but fail to describe many binary MGs, notably metal–metalloid glasses, where the chemical SRO is pronounced. The stereochemically defined model proposed later[4,5], in contrast, stipulates that the local unit (such as nearest neighbours) in amorphous alloy has the same type of structure as their crystalline compounds with similar composition. The general applicability of this model is still being debated, as experimental evidence has not yet been conclusive. Even less understood is the medium-range order (MRO), which can be defined as the next-level structural organization beyond the SRO[6], for example, how the local structural 'units' are connected and arranged to fill three-dimensional (3D) space. The characteristics of the MRO remain one of the most important outstanding questions[7,8] in MG research. Taking the earlier models further, a recent model[9] proposes face-centred cubic (f.c.c.) packing of overlapping clusters as the building scheme for MG structures. The underlying principle is the efficient filling of space[9,10]. Clearly, there is a pressing need for an in-depth reality check of these previous structural concepts, and for establishing a realistic structural picture of MGs.

## Obtaining the 3D structure of metallic glasses

We set out to solve the 3D structure of MGs rather than proposing models *a priori*. To achieve a realistic description of the structure, we used experimental and computational techniques that allow us to explicitly consider chemical effects and atomic relaxations in realistic many-body interactions of 'soft atoms' (rather than hard spheres), which are absent in earlier models. Atomic coordinates from the 3D structure were then used for more detailed analysis of structural features, from which basic principles underlying the short-to-medium-range order could be extracted. As illustrated in detail below, our results validate several of the earlier concepts regarding the SRO and efficient packing, specify the particular topologies of cluster-like

entities, and suggest a fundamentally new cluster packing scheme that constitutes the MRO. For completeness, we also illustrate how the solute atoms arrange themselves in alloys with enriched solute concentrations.

**Metallic glass structure from XRD, EXAFS and RMC.** We started by analysing a model MG, Ni₈₀P₂₀, using structural information acquired through synchrotron X-ray measurements. In addition to wide-angle X-ray scattering (Fig. 1a), extended X-ray absorption fine structure (EXAFS) experiments have been used as the species-specific probe to provide local coordination information (see Fig. 1 and the Methods). Unlike previous work that dealt mostly with the one-dimensional pair distribution functions, we focused on the 3D atomic configuration (atomic positions, density) reconstructed using the reverse Monte Carlo (RMC)[11,12] method, which produced the excellent fits to the experimental spectra in Fig. 1 (see Methods). The final configuration was double-checked by comparing the X-ray absorption near-edge structure (XANES) patterns calculated from the RMC structure (Fig. 1d) with that observed in the X-ray absorption experiments (shown in Supplementary Fig. S1 but not used in RMC fitting). We also confirmed that the one-dimensional partial pair distribution functions obtained from the RMC configuration are in satisfactory agreement with those obtained before from neutron isotope experimental measurements[13] (see the comparison in Supplementary Fig. S2).

**Structure from ab initio molecular dynamics simulations.** We also pursued the 3D MG structure via a completely independent route: *ab initio* molecular dynamics simulations[14,15]. Here the atomic forces are determined on the basis of first-principles calculations without the need for any experimental data or empirical potentials (details in the Methods[16–21]). The *ab initio* calculations allowed us not only to obtain and analyse the static amorphous structure, but also to monitor the structural evolution during the liquid cooling process. More importantly, the *ab initio* modelling enabled us to deduce a general trend by systematically comparing a number of MG systems with different chemical make-ups (such as transition metal (TM)–TM and TM–metalloid), different atomic size ratios and different levels of solute concentrations.

[1]Department of Materials Science and Engineering, Johns Hopkins University, Baltimore, Maryland 21218, USA. [2]National Institute of Standards and Technology, Gaithersburg, Maryland 20899, USA. [3]High-Temperature Materials Laboratory, Oak Ridge National Laboratory, Oak Ridge, Tennessee 37831, USA.

Figure 2 illustrates the evolution of the reduced radial distribution functions (RRDFs) as a function of temperature during the cooling of the *ab initio* Ni–P system. The development of SRO with decreasing temperature is clearly observed from the structure developed in the second peak. The partial RRDFs of the final 300 K configuration (purple curve) agree remarkably well with those directly measured from experiments[13] (orange dots). Furthermore, the EXAFS spectra in Fig. 1 (as well as the XANES spectra in Supplementary Fig. S1) obtained using first-principles calculations[12] for the 300 K *ab initio* configurations also exhibit an excellent match with the experimental data. These validations lend strong support to the use of the

configuration obtained from the 'virtual' quenching experiments for structural analysis of the 3D atomic packing. An additional check for both the RMC and molecular dynamics configurations is that their mass (or atomic) densities are all within 1 to 2% of the experimentally measured value for the Ni–P (and 0.7% for Ni–B) discussed below) MG.

### Structural analysis based on Voronoi tessellation

The atomic positions in both the RMC and *ab initio* molecular dynamics configurations can then be used, and compared, to unravel the short-to-medium-range details. Our first objective was to identify the possible presence of building blocks, or 'clusters'. The first step was to resolve the local nearest-neighbour coordination. The coordination number (CN) can be determined unambiguously by using the Voronoi tessellation method[23-26], which also characterizes the local atomic environment. We use the Voronoi index $(n_3, n_4, n_5, n_6, ....)$, where $n_i$ denotes the number of $i$-edged faces of the Voronoi polyhedron and $\sum n_i$ is the total CN, to designate and differentiate the type of the coordination polyhedron surrounding a centre solute atom. For example, tri-capped trigonal prism packing (TTP) corresponds to a Voronoi index of $\langle 0,3,6,0 \rangle$, while a mono-capped square archimedean antiprism (slightly distorted from the TTP) has a Voronoi index of $\langle 0,5,4,0 \rangle$ (see Supplementary Fig. S3).

In the Ni–P glass the solute P was found to be coordinated in the first neighbouring shell by Ni atoms only, and the statistics of the Voronoi analysis indicated that the average first-neighbour CN of the P solute is 10.5 for the *ab initio* configuration, and 10.6 for the RMC model, with very similar distribution for the two 3D configurations (see the distribution in Fig. 3 for the *ab initio* configuration). Such a CN would seem to be larger than was determined in previous

RDF work[7,13] by counting the number of atoms belonging to the 'first shell', which is very sensitive to the predefined cut-off distance. However, we confirmed that the results are consistent, as the CN turned out to be 9.4 when we used a cut-off distance of 2.8 Å in the RDF (Fig. 2), in good agreement with previous analyses of TM–metalloid MGs[7,13].

### Dependence of local packing on atomic size ratio

To observe general features and trends, we analysed a number of model MGs using *ab initio* molecular dynamics simulations. These structural configurations are validated by comparing the calculated RRDFs with the experimentally measured ones (see below). Owing to the different atomic size ratios, the CN distribution of these MGs shifts consistently, as shown in Fig. 3. The solvent atoms surrounding the centre solute atom apparently form different types of coordination polyhedra in these various systems. As opposed to Pauling's rule of parsimony[27], which states that the number of the chemically different environments of an (ionic) compound tends to be small (for example, even the most complex of silicates minerals typically has only three to four different kinds of coordination polyhedra[28]), the solute-centred polyhedra in each of the MGs studied involve a large number (as many as a few hundred) of coordination polyhedron types. Such diversity has previously been reported in classical molecular dynamics simulations of model systems[23,29], and has recently been enumerated[25,26]. This finding suggests that the local arrangements cannot be modelled by a uniquely prescribed stereochemical structure. This conclusion was also corroborated by our analysis of the rather broad bond-angle distribution (see Supplementary Fig. S4).

On the other hand, despite the large number of the geometrically distinct polyhedron types, certain polyhedra appeared with high frequencies (20–40%; see Fig. 4). A closer inspection suggests that they are Kasper polyhedra, which are the deltahedra that involve the minimum number of disclinations[30,31]. The atomic packing configurations of different Kasper polyhedra are shown in Fig. 3. In the Ni–P glass, the percentages of the Z10 (Z = CN) Kasper polyhedron (the bi-capped square archimedean antiprism, BSAP, with Voronoi index $\langle 0,2,8,0 \rangle$), and the Z11 Kasper polyhedra (with $\langle 0,2,8,1 \rangle$) are

16.2% and 10.6%, respectively, while in the $Ni_{81}B_{19}$ MG, the Z9 Kasper polyhedron (TTP, with $\langle 0,3,6,0 \rangle$) and the Z10 Kasper polyhedra are dominant (at 17.8% and 7.1%, respectively). In comparison, prominent icosahedral local order is found in the $Zr_{84}Pt_{16}$ MG, where the occurrences of the Z12 and Z11 Kasper polyhedra are 14.1% and 9.0%, respectively. Therefore, it is evident that the Kasper polyhedron SRO is the main underlying topological SRO in the MGs.

The preference for a particular type, as seen in Fig. 3 together with the shift of the main peak, is controlled by the effective atomic size ratio between the solute and solvent atoms, $R^*$. With decreasing $R^*$, the preferred polyhedra type changes from the Frank–Kasper[32] type (for $R^* > 1.2$) to the icosahedral type ($R^* \approx 0.902$, as for Zr–Pt with $R^* \approx 0.90$), and then to the BSAP type ($R^* \approx 0.835$, as in Ni–P with $R^* \approx 0.78$), and then to the TTP type ($R^* \approx 0.732$, as in Ni–B with $R^* \approx 0.69$); see Figs 3 and 4. As pointed out above, some MGs, notably TM–metalloid systems (Ni–B, Pd–Si and so on), indeed exhibit the TTP local order, similar to that in corresponding crystalline compounds[33]. But this should be understood as a geometrical consequence and only specific to a small number of MGs that meet the $R^*$ requirement for the formation of TTP ($R^* \approx 0.732$). Our results not only validate the important role of the relative size
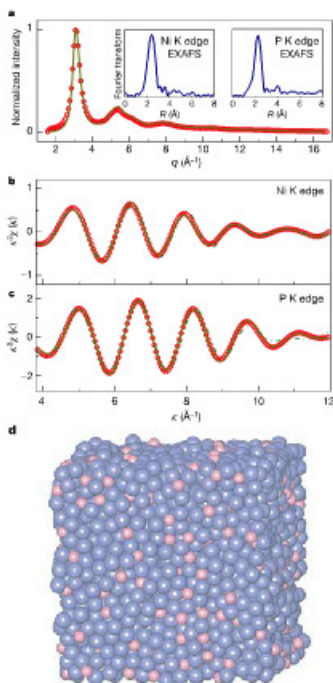


**Figure 1 | Reverse Monte Carlo modelling to reproduce the experimental X-ray diffraction and absorption data. a,** Solid lines are the experimental XRD and Fourier-transformed EXAFS spectra for the $Ni_{80}P_{20}$ amorphous alloy. The circles are for the XRD pattern calculated for the eventual RMC configuration. **b, c,** The solid lines present the inverse Fourier transforms of the first peaks in the Fourier-transformed EXAFS data in **a.** $\chi(\kappa)$ is the EXAFS, where $\kappa$ is the photoelectron wavevector. $R$ is the distance between atoms. The EXAFS spectra calculated for the RMC configuration (circles) and for the *ab initio* molecular dynamics configuration (green line) are in good agreement with the experimental data. **d,** A view of the final RMC configuration. The blue and pink balls represent Ni and P atoms, respectively.
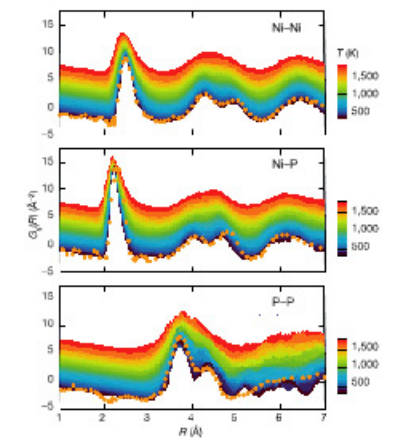


**Figure 2 | The evolution of partial RRDFs of the $Ni_{80}P_{20}$ liquid observed in *ab initio* molecular dynamics simulations.** The partial RRDFs, $G_{ij}(R)$, change as a function of temperature during the cooling and glass formation of the $Ni_{80}P_{20}$ liquid. $G_{ij}(R) = 4\pi R[\rho_{ij}(R)/c_j - \rho_0]$, where $\rho_{ij}(R)$ is the atomic density of the $j$ atom at distance $R$ from an $i$ atom, and $\rho_0$ is the mean atomic density. The experimental data for this glass are also shown for comparison (orange circles, redrawn from ref. 13).
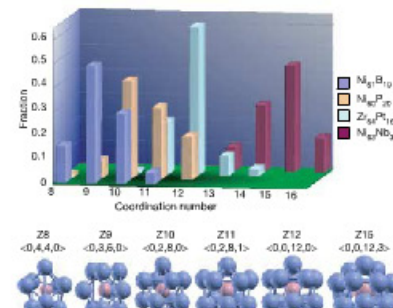


**Figure 3 | CN distribution of the solute atoms in several representative MGs, obtained from *ab initio* calculations.** The average CN changes with the effective atomic size ratio, and for each glass the majority of the solute atoms (>75% of total) have two dominant CNs. Also shown are the Kasper polyhedra corresponding to the different CNs. The Kasper polyhedra are the dominant coordination polyhedra in the relaxed MGs.
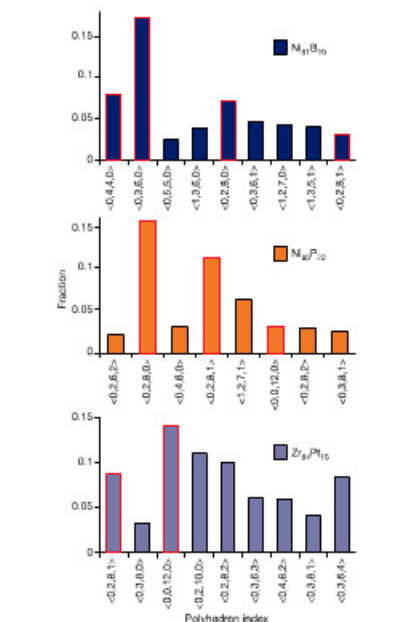


**Figure 4 | The occurrences of different coordination polyhedra (with different Voronoi indices) of the solute atoms in the MGs.** The bars outlined in red show the frequency of the dominant Kasper polyhedra. Note that only the polyhedra with a population of >2% are shown.

between the solute and solvent atoms[3,33,34], but also explicitly specify the packing topologies for the various CNs.

## Packing of quasi-equivalent clusters

For each one of the MGs, the several types of local coordination polyhedra specified above are geometrically different, not identical in topology and CN. They can nevertheless be considered quasi-equivalent, or cluster-like units for a given glass, supporting the framework of cluster packing[9]. This is because, first, the solute-centred 'clusters' in Fig. 5 (dashed circles) have similar sizes, as seen from their narrow volume distribution. Second, as discussed above, the CN of the solute at centre has a relatively small variance around an average controlled by $R^*$, and the polyhedra can be considered distortions of certain specific types of Kasper polyhedra. That the CN is not a unique integer for a given glass, as is sometimes designated in idealized hard-sphere models[9,10], is not surprising. This moderate CN distribution (or a range of quasi-equivalent clusters) is a natural consequence of strain relaxation in an MG to allow for more comfortable packing of 'soft' atoms (many-body interactions rather than touching hard spheres all of the same size), in the entire solid (not just one nearest-neighbouring shell as idealized in some models[10]). Such arrangements will permit more flexibility for efficient filling of the entire 3D space, with reduced energy (see below).

We point out that the formation of the local solute-centred coordination polyhedra is a manifestation of the strong chemical SRO favouring unlike bonds. An examination of the calculated electronic structures demonstrates the strong chemical affinity between the TM and metalloid, resulting from the partially covalent nature of the bonding that is still mostly non-directional. In the TM–TM glasses, we often observed non-additive pair interaction, arising from the charge transfer and screening of $d$ electrons. Chemical SRO is well known in these TM–metalloid and TM–TM systems, and is usually one of the prerequisites for the easy formation of MGs[35].

Owing to the bond non-additivity, the effective $R^*$ is different from that estimated from their Goldschmidt atomic radii. In the literature, the absence of the direct solute–solute contacts is termed 'solute–solute avoidance'[7]. In other words, in the partial RRDFs of the solutes (see TM–metalloid glasses in Fig. 2 and Supplementary Fig. S7), there is little or no solute–solute pair correlation peak at the nearest-neighbour position. The chemical SRO—that is, the fact that the solute atom sits in the centre defining the quasi-equivalent clusters—sets the stage for the formation of the type of MRO discussed below.

**The solute–solute correlations and MRO.** With the 'quasi-equivalent cluster' defined in this way, and after illustrating the intra-cluster packing (topological and chemical SRO), the next issue we discuss is the correlation among solute atoms (and solute-centred clusters). This addresses the important question of how the clusters are connected and packed to fill the 3D space, giving rise to MRO.

We now describe the (dense) geometric/topological packing of the quasi-equivalent clusters. To differentiate several important candidate schemes, we make use of the common-neighbour analysis[36]. In the present study, the quasi-equivalent clusters were treated as rigid balls, each occupying the volume of the coordination polyhedron of the solute atom at centre. As shown in Fig. 5a, in the $Ni_{81}B_{19}$, $Ni_{80}P_{20}$ and $Zr_{84}Pt_{16}$ systems, the solute-centred clusters are packed with appreciable icosahedral topological order, as evidenced from the prominent presence of the 555 icosahedral signature pairs, as well as the 544 and 433 pairs (the 555 index represents a perfect fivefold ring of common neighbours and the latter two correspond to the defective/distorted rings[36]). Very similar results were found in the RMC configuration of the Ni–P system; see Supplementary Fig. S5. The 421 and 422 indices, signatures for close-packed face-centred cubic (f.c.c.) and hexagonal close-packed (h.c.p.), are insignificant.

Note that the common-neighbour analysis indices above reveal the presence of fragments (see Supplementary Fig. S5) of icosahedra, but not necessarily any perfect icosahedra. This can be termed 'icosahedral ordering', a term often used to describe local topological SRO in undercooled liquids[37,38] and glasses[11] (such as the Zr–Pt glass discussed here). Here it is short range for the packing of clusters, but already medium range from the standpoint of atomic (solute) correlation beyond one cluster. The icosahedral-type MRO (cluster) ordering is a general feature regardless of the types of SRO inside the clusters, as shown in Fig. 5b–d, where the intracluster packing varies from the TTP order in Ni–B, to the BSAP in Ni–P, to the icosahedral SRO in Zr–Pt, as illustrated above. The tendency for icosahedral order is not surprising, as in all these alloy systems, each of the clusters has an average of 12–13 neighbouring clusters of about the same size (see Supplementary Fig. S6 for the cluster–cluster common-neighbour analysis). This indicates dense packing, hence favouring f.c.c., h.c.p., or icosahedral order. The icosahedral packing scheme preferring fivefold symmetry is in fact intrinsically associated with the dense packing in amorphous materials, and is not uncommon in the literature for the packing of small clusters or particles[36,39–41].

We stress that the $ab$ $initio$ calculated structures produce partial RRDFs in very good agreement with the experimental ones: see the excellent match of the RRDFs, Supplementary Fig. S7. Note also in Supplementary Fig. S7 that the splitting B–B first correlation peak seen in the experimental RRDF of Ni–B (and solute–solute correlation in some other TM–metalloid systems as well) was not reproduced by the previously proposed model assuming f.c.c. packing of overlapping equal-sized clusters[9]. This strongly suggests that the icosahedral fivefold packing is a more realistic ordering pattern of cluster–cluster connection in MGs. Our solute–solute–solute bond-angle analysis corroborates this conclusion. The cluster-connection diagrams in Fig. 5b–d for the several MGs illustrate the specific packing/connection schemes of the quasi-equivalent clusters, through the sharing of edges, faces and vertices. In fact, these different sharing schemes explain the different solute–solute distances that lead to the splitting in the peaks in the respective solute–solute partial RRDFs (Supplementary Fig. S7). Similar schemes for the communication among clusters were predicted in Gaskell's

model for the connection of TTP clusters[7], but in a random chain configuration.

**Cavities.** As suggested in the previously proposed model of f.c.c. packing of stoichiometric clusters[9], the packing of quasi-equivalent clusters may leave behind some 'cavities'. They can be identified by locating spaces with relatively low electron charge densities. We found that the larger cavities are associated with multiple clusters, and have a correlation with the cluster arrangement (See Supplementary Fig. S8). The location of the larger cavities resembles Bernal's canonical holes[2], if regarding the clusters as hard spheres. The analysis of the size and distribution of the cavities would have implications for glass-forming ability, especially when additional solute species with different sizes are introduced to fill such cavities to form bulk MGs[42], as well as in the understanding of transport mechanism, glass transition, shear transformation in plastic flow, and the structure factors in scattering experiments (for example, the pre-peaks observed in some systems). But this topic is beyond the scope of this paper.

## Strings and networks

The icosahedral ordering of single-solute-centred quasi-equivalent clusters is an efficient packing scheme, but is not the only type of MRO. When the concentration of the solute species increases to beyond the level at which each of all the solute atoms can be encaged in a single-solute-centred cluster, neighbour contact between solute atoms becomes inevitable. This produces direct bonding between like atoms. It is tempting to surmise that the excess solute atoms might be located at the interstitial 'vacancies' of the densely packed clusters[9]. But we found instead that a different kind of building unit emerges. In our $ab$ $initio$ calculated systems, the connection between solute atoms takes the form of 'strings'. For instance, two neighbouring solute atoms form an isolated pair surrounded by the solvent atoms, and the resulting configuration may be termed 'extended clusters'. In the $Zr_{80}Pt_{20}$ metallic glass (Fig. 6a) a solute pair is seen to have a total CN of ~17. Similarly, string-like solute atoms are apparent in systems with higher solute concentrations (for example, Fig. 6b for amorphous $Al_{75}Ni_{25}$). The dense packing of the extended clusters, via edge-, vertex-, or face-sharing, constitutes the second type of MRO. This type of packing becomes significant when the solute concentration reaches roughly 20–30%, depending on the $R^*$ ratio.

As the number of the direct bonds among solutes further increases with enriched solute concentration, more and more solute–solute contacts become unavoidable. A pronounced first-neighbour solute–solute pair correlation peak in the partial RRDFs emerges, as measured before for glasses such as Ni–Nb (ref. 43; Supplementary Fig. S7). When the solute interconnection percolation threshold is eventually reached, a network of the solute atoms takes form (Fig. 6c for amorphous $Ni_{63}Nb_{37}$). The string- or ring-like interconnection reduces the number of like bonds (increases the number of unlike bonds), when compared to aggregated solute atoms, leading to energy reduction. This is illustrated in Supplementary Fig. S9: when the $Zr_{70}Pd_{30}$ glass[44] is cooled from 1,800 to 300 K, the solute–solute connection becomes more network-like. The acute (solute–solute–solute) bond angles observed at high temperatures disappear, reflecting the tendency to order the solute atoms in string-like and ring-like medium-range arrangements that reduce the number of like bonds. The solute–solute CN in this open and extended connection is generally no more than 3 to 7. This network-type arrangement of the solute atoms leads to a much-involved third type of MRO. The concept of connected random network has previously been proposed in ref. 45. We have thus uncovered a whole spectrum of atomic packing schemes, which vary not only with $R^*$ but also with solute concentration.

## Limitations of models

We should briefly discuss the inherent limitations of the modelling techniques. The rapid quenching used for the $ab$ $initio$ systems did
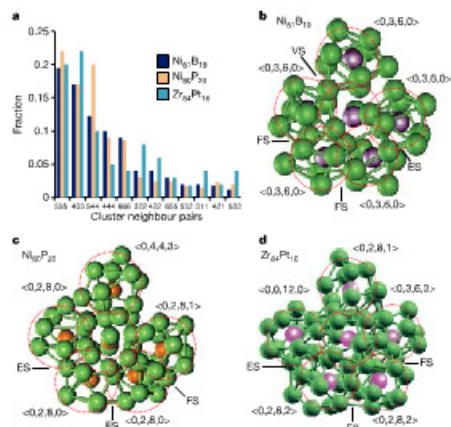


**Figure 5 | The packing of the solute-centred quasi-equivalent clusters, showing their MRO.** a, The cluster common-neighbour analysis showing that the local clusters in the MGs exhibit icosahedral type ordering. The typical cluster connections, exhibiting the fivefold symmetry, are detailed for $Ni_{81}B_{19}$, $Ni_{80}P_{20}$ and $Zr_{84}Pt_{16}$ in b, c and d, respectively. For each local cluster, the Voronoi index is given to indicate its identity. FS, ES and VS denote face-sharing, edge-sharing and vertex-sharing, respectively. The red dashed circles delineate the clusters and suggest the quasi-equivalence of the clusters. The bonds for the centre cluster are not connected for clarity.
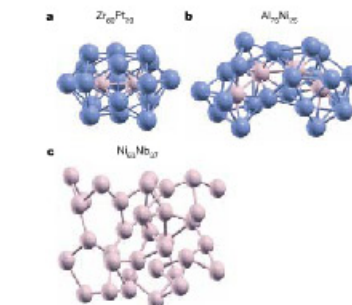


**Figure 6 | Configurations of solute atoms at increasing solute concentrations.** a, Extended clusters in the form of 'lone pairs' (here, two atom-sharing icosahedra with CN = 17) in the $Zr_{80}Pt_{20}$ MG. b, Extended clusters in the form of 'strings' in the $Al_{75}Ni_{25}$ MG. The dense packing of such 'extended' clusters constitutes the second type of MRO. c, The solute network formed in the $Ni_{63}Nb_{37}$ MG, in which the solute concentration is high. The network-like arrangement of the solute atoms gives rise to a different, third type of MRO.
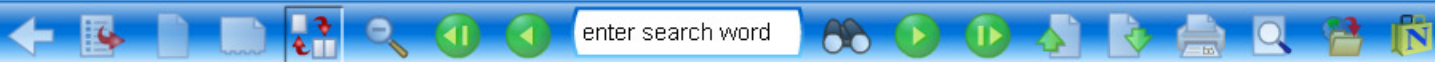
not appear to suppress the development of ordering, as the agreement between the calculated (at ultrahigh quenching rates) and experimental (for glasses obtained at lower cooling rates) partial RRDFs is remarkable (Fig. 2 and Supplementary Fig. S7). This shows that the pair correlations established in our calculated systems are similar to those in experimental samples, for the SRO and the MRO on the short-range side[46] examined here (the experimental data available for validation are for the range below 8 Å, although in general MRO may extend up to approximately 2 nm; see Fig. 2 and Supplementary Fig. S7). We also compared the structure of the $Ni_{80}P_{20}$ MG obtained at two different quench rates (see Methods) and found no obvious difference.

To observe the effects of the small size of the system and the imposed periodic boundary conditions, we examined different sizes up to 2.2 nm for the edge length of the cube, and also modelled the $Ni_{80}P_{20}$ glass using a large system of 4,000 atoms. In the latter case, however, classical molecular dynamics simulations[36] involving empirical or hypothetical interatomic potentials had to be used (binary mixture of Lennard-Jones particles using the modified Kob–Andersen interatomic potentials[47]). All the results are consistent with what we have presented above. This suggests the particular MRO is not due to a small system under periodic boundary conditions. However, it is certainly true that one prefers slower cooling rates to allow the system to survey the energy landscape more thoroughly, attaining lower energy states through increased structural ordering. While SRO may converge fast, the degree and extent of the MRO development may be affected by the rapid computer quench in small systems (our RMC system is much larger, but the Monte Carlo procedure used in RMC also favours randomization). Therefore, the SRO and MRO we report here could be underestimates; the ordering actually present in the (more structurally relaxed) MGs should be at least as much.

## METHODS

**EXAFS data.** $Ni_{80}P_{20}$ foils with thicknesses of up to 10 μm were prepared using electroplating from Brenner-type baths onto Cu foils, which were etched away after deposition. X-ray diffraction (XRD), transmission-mode Ni K-edge and fluorescence-mode P K-edge EXAFS data were collected at beamline X14A and X15B, respectively, of the National Synchrotron Light Source (NSLS) at Brookhaven National Laboratory (BNL). The EXAFS data were Fourier-transformed into real space after pre-edge and post-edge background subtractions. The first peak up to ~3.5 Å in real space corresponding to the nearest-neighbor shell was inverse-Fourier-transformed back into κ space. Through the Fourier-filtering procedure, the simple single-scattering signal from local environment around the absorbing element was decomposed from the total EXAFS signal and can be analysed separately using standard EXAFS formula and theoretical amplitude and phase functions.

**RMC modelling.** RMC modelling, based on experimental XRD and Fourier-filtered EXAFS data above, was employed to reconstruct 3D atomic configuration in the amorphous alloy without any predetermined hypothetical structural models. The RMC system used typically 4,000 atoms. The metropolis algorithm is used in the RMC code and the error between the simulated and experimental data are analogous to the 'potential energy' in conventional Monte Carlo simulations. An atomic guess configuration is generated by randomly moving or exchanging atoms. The structure is improved by reducing the fitting residual while the deviation serves as 'temperature' and is slowly 'cooled' following the simulated annealing scheme. We confirmed that the output structure of our RMC modelling, upon matching the experimental input after ~$10^7$ running steps, is independent of the starting configuration: the initial configuration can be either a 3D lattice or a random structure under appropriate constraints and periodic boundary conditions.

***Ab initio* simulations.** For the *ab initio* molecular dynamics simulations, canonical NVT (constant number, volume, temperature) ensembles are used applying the Vienna *ab initio* simulation package[15]. The temperature was controlled using the Nose–Hoover thermostat[16]. 100–200 atoms with the desirable composition, are arranged in a cubic box with periodic boundary conditions. The simulation was performed on the Γ point only. Projected augmented planewaves (PAW)[18,19] with the Perdew–Wang exchange-correlation potentials[20] have been adopted. The valence state of each element has been previously defined in the provided PAW pseudopotentials. One important

quantity throughout the simulations is the determination of the density of the systems. For this purpose, the ensemble was melted and equilibrated at high temperatures (1,800–2,200 K) for 2,000 timesteps, with each timestep of 5 fs. The conjugated gradient method was used to obtain the inherent structure[21] of the liquid. The density was adjusted to correspond to the zero pressure of the inherent structure of the liquid. The quenching rate used to obtain the various glass systems is in the range of 200 to 20 K per 1,000 timesteps ($4 \times 10^{13}$ to $4 \times 10^{12}$ K s$^{-1}$). Alloys selected include several TM–metalloid ($Ni_{80}P_{20}$, $Ni_{80}B_{20}$), TM–TM ($Zr_{84}Pt_{16}$, $Zr_{80}Pt_{20}$, $Zr_{77}Pd_{23}$, $Ni_{63}Nb_{37}$) and metal–TM ($Al_{75}Ni_{25}$, $Al_{25}Zr_{75}$) systems.

**Voronoi tessellation.** Details about the Voronoi tessellation method can be found in references[45]. In constructing the Voronoi polyhedra, we removed those surfaces with area less than 1% of the total area of the polyhedron surfaces. By doing so, the degeneracy problem and the effects of thermal vibration are minimized. For the cluster–cluster common neighbour analysis, a pre-set threshold length for the nearest neighbour distance would introduce an ambiguity. We used instead the Voronoi tessellation method to determine the cluster neighbours. This was done by tessellating the space into 'regions of the solute atoms', and two neighbouring solute atoms represent two connecting clusters. The common-neighbour analysis was then carried out on the cluster neighbours identified. In the bond-angle analysis, the bond angle refers to the included angle between two atoms in the first coordination shell and the atom in the centre of the cluster.

1. Bernal, J. D. Geometry of the structure of monatomic liquids. *Nature* **185**, 68–70 (1960).
2. Bernal, J. D. The structure of liquids. *Proc. R. Soc. Lond. A* **280**, 299–322 (1964).
3. Greer, A. L. *Intermetallic Compounds—Principles and Practice* Vol. 1 (eds Westbrook, J. H. & Fleischer, R. L.) 731–754 (Wiley, New York, 1995).
4. Gaskell, P. H. A new structural model for transition metal–metalloid glasses. *Nature* **276**, 484–485 (1978).
5. Gaskell, P. H. A new structural model for amorphous transition metal silicides, borides, phosphides and carbides. *J. Non-Cryst. Solids* **32**, 207–224 (1979).
6. Elliott, S. R. *Physics of Amorphous Materials* 2nd edn, 139–151 (Longman, London, 1990).
7. Gaskell, P. H. *Amorphous Metals* (eds Matyja, H. & Zielinski, P. G.) 35–57 (World Scientific Publishing, Singapore, 1985).
8. Gaskell, P. H. Medium-range structure in glasses and low-Q structure in neutron and X-ray scattering data. *J. Non-Cryst. Solids* **351**, 1003–1013 (2005).
9. Miracle, D. B. A structural model for metallic glasses. *Nature Mater.* **3**, 697–702 (2004).
10. Miracle, D. B., Sanders, W. S. & Senkov, O. N. The influence of efficient atomic packing on the constitution of metallic glasses. *Phil. Mag. A* **83**, 2409–2428 (2003).
11. McGreevy, R. L. Reverse Monte Carlo modeling. *J. Phys. Cond. Matter* **13**, R877–R913 (2001).
12. Luo, W. K. *et al.* Icosahedral short-range order in amorphous alloys. *Phys. Rev. Lett.* **92**, 145502 (2004).
13. Lamparter, P. Reverse Monte-Carlo simulation of amorphous $Ni_{80}P_{20}$ and $Ni_{81}B_{19}$. *Phys. Scr.* **T57**, 72–78 (1995).
14. Payne, M. C., Teter, M. P., Allan, D. C., Arias, T. A. & Joannopoulos, J. D. Iterative minimization techniques for ab initio total-energy calculations: molecular dynamics and conjugate gradients. *Rev. Mod. Phys.* **64**, 1045–1097 (1992).
15. Kresse, G. & Hafner, J. Ab initio molecular dynamics for liquid metals. *Phys. Rev. B* **47**, 558–561 (1993).
16. Allen, M. P. & Tidesley, D. J. *Computer Simulation of Liquids* (Clarendon, Oxford, 1989).
17. Kresse, G. & Furthmüller, J. Efficiency of ab-initio total energy calculations for metals and semiconductors using a plane-wave basis set. *Comput. Mater. Sci.* **6**, 15–50 (1996).
18. Blöchl, P. E. Projector augmented-wave method. *Phys. Rev. B* **50**, 17953–17979 (1994).
19. Kresse, G. & Joubert, D. From ultrasoft pseudopotentials to the projector augmented-wave method. *Phys. Rev. B* **59**, 1758–1775 (1999).
20. Wang, Y. & Perdew, J. P. Correlation hole of the spin-polarized electron gas, with exact small-wave-vector and high-density scaling. *Phys. Rev. B* **44**, 13298–13307 (1991).
21. Stillinger, F. H. & Weber, T. A. Packing structures and transitions in liquids and solids. *Science* **225**, 983–989 (1984).
22. Ankudinov, A. L., Ravel, B., Rehr, J. J. & Conradson, S. D. Real-space multiple-scattering calculation and interpretation of X-ray-absorption near-edge structure. *Phys. Rev. B* **58**, 7565–7576 (1998).
23. Finney, J. L. Random packing and the structure of simple liquids. *Proc. R. Soc. A* **319**, 479–493 (1970).
24. Finney, J. L. Modeling structures of amorphous metals and alloys. *Nature* **266**, 309–314 (1977).
25. Borodin, V. A. Local atomic arrangements in polytetrahedral materials. *Phil. Mag. A* **79**, 1887–1907 (1999).
26. Borodin, V. A. Local atomic arrangements in polytetrahedral materials. II. Coordination polyhedra with 14 and 15 atoms. *Phil. Mag. A* **81**, 2427–2446 (2001).
27. Pauling, L. The principles determining the structure of complex ionic crystals. *J. Am. Chem. Soc.* **51**, 1010–1026 (1929).
28. O'Keeffe, M. & Navrotski, A. (eds) *Structure and Bonding in Crystals* (Academic, New York, 1981).
29. Qi, D. W. & Wang, S. Icosahedral order and defects in metallic liquids and glasses. *Phys. Rev. B* **44**, 884–887 (1991).
30. Doye, J. P. K. & Wales, D. J. The effect of the range of the potential on the structure and stability of simple liquids: from clusters to bulk, from sodium to $C_{60}$. *J. Phys. B* **29**, 4859–4894 (1996).
31. Nelson, D. R. Order, frustration, and defects in liquids and glasses. *Phys. Rev. B* **28**, 5515–5535 (1983).
32. Frank, F. C. & Kasper, J. S. Complex alloy structures regarded as sphere packings. I. Definitions and basic principles. *Acta Crystallogr.* **11**, 184–190 (1958).
33. Watson, R. E. & Bennett, L. H. Crystalline and glassy phases of transition-metal–metalloid systems. *Phys. Rev. B* **43**, 11642–11652 (1991).
34. Egami, T. & Waseda, Y. Atomic size effect on the formability of metallic glasses. *J. Non-Cryst. Solids* **64**, 113–134 (1984).
35. Hafner, J. Theory of the formation of metallic glasses. *Phys. Rev. B* **21**, 406–426 (1980).
36. Clarke, A. S. & Jónsson, H. Structural changes accompanying densification of random hard-sphere packings. *Phys. Rev. E* **47**, 3975–3984 (1993).
37. Jónsson, H. & Anderson, C. Icosahedral ordering in the Lennard-Jones liquid and glass. *Phys. Rev. Lett.* **60**, 2295–2298 (1988).
38. Kelton, K. F. *et al.* First X-ray scattering studies on electrostatically levitated metallic liquids: demonstrated influence of local icosahedral order on the nucleation barrier. *Phys. Rev. Lett.* **90**, 195504 (2003).
39. Manoharan, V. N., Elsesser, M. T. & Pine, D. J. Dense packing and symmetry in small clusters of microspheres. *Science* **301**, 483–487 (2003).
40. Caspar, D. L. D. & Klug, A. Physical principles in the construction of regular viruses. *Quant. Biol.* **27**, 1–24 (1962).
41. Zandi, R., Reguer, D., Bruinsma, R. F., Gelbart, W. M. & Rudnick, J. Origin of icosahedral symmetry in viruses. *Proc. Natl Acad. Sci. USA* **101**, 15556–15560 (2004).
42. Greer, A. L. Metallic glasses. *Science* **267**, 1947–1953 (1995).
43. Lamparter, P. Structure of metallic glasses. *Phys. Scr.* **T57**, 45–63 (1995).
44. Kramer, M. J. & Sordelet, D. J. Polymorphism in the short-range order of $Zr_{71}Pd_{10}$ metallic glasses. *J. Non-Cryst. Solids* **351**, 1586–1593 (2005).
45. Dubois, J. M., Gaskell, P. H. & Le Caer, G. A model for the structure of metallic glasses based on chemical twinning. *Proc. R. Soc. A* **402**, 323–357 (1985).
46. Ohkubo, T. & Hirotsu, Y. Electron diffraction and high-resolution electron microscopy study of an amorphous $Pd_{82}Si_{18}$ alloy with nanoscale phase separation. *Phys. Rev. B* **67**, 094201 (2003).
47. Kob, W. & Andersen, H. C. Testing mode-coupling theory for a supercooled binary Lennard-Jones mixture: The van Hove correlation function. *Phys. Rev. E* **51**, 4626–4641 (1995).